Reconstruction of Viscosity Maps in Ultrasound Shear Wave Elastography

Manish Bhatt, Marine A. C. Moussu, Boris Chayer, François Destrempes, Marc Gesnik, Louise Allard, An Tang, and Guy Cloutier, *Senior Member, IEEE*

***Abstract*— Change in viscoelastic properties of biological tissues may often be symptomatic of dysfunction that can be correlated with tissue pathology. Shear wave (SW) elastography is an imaging method mainly used to assess stiffness but with the potential to measure viscoelasticity of biological tissues. This can enable tissue characterization and, thus, can be used as a marker to improve the diagnosis of pathological lesions. In this study, a frequency-shift method-based framework is presented for the reconstruction of viscosity by analyzing the spectral properties of acoustic radiation force-induced SWs. The aim of this study was to investigate the feasibility of viscosity reconstruction maps in homogeneous as well as heterogeneous samples. Experiments were performed in four *in vitro* phantoms, two *ex vivo* porcine liver samples, two *ex vivo* fatty duck liver samples, and one *in vivo* fatty goose liver. Successful viscosity maps were reconstructed in homogeneous and heterogeneous phantoms with embedded mechanical inclusions having different geometries. Quantitative values of viscosity obtained for two porcine liver tissues, two fatty duck liver samples, and one goose fatty liver were (mean ± SD) 0.61 ± 0.21 and 0.52 ± 0.35, 1.28 ± 0.54 and 1.36 ± 0.73, and 1.67 ± 0.70 Pa.s, respectively.**

***Index Terms*— Liver, rheology, shear wave (SW) elastography, spectral shift, viscoelasticity, viscosity reconstruction.**

I. Introduction

SHEAR wave (SW) elastography is a technology that uses clinical ultrasound (US) to noninvasively assess the mechanical properties of soft tissues [1]–[6]. This technique is based on the propagation of SWs in biological tissues and relies on the equations of wave propagation to infer tissue properties. Popular methods to generate SWs within a target tissue are acoustic radiation force impulse (ARFI) imaging [1], [7]–[9] and supersonic shear imaging (SSI) techniques [10]–[13], in which the target tissue is imaged with a remote US probe that first generates an acoustic radiation force-induced tissue motion and then tracks this motion using the US-based motion tracking algorithms. In general, the aim is to indirectly measure the stiffness of the tissue by monitoring the propagation of SWs inside it. SWs are known to propagate faster in stiffer tissues and slower in softer media. Clinical applications of SW elastography include a diagnostic examination of numerous soft-tissue organs, such as the liver, breast, gastrointestinal tract, thyroid, lymph nodes, and tendons [13]–[15]. Different stiffness scores for diagnostic interpretation of pathological conditions have been proposed for clinical use [15].

The stiffness, quantified by the shear modulus (G), of a purely elastic medium can be directly related to the SW speed (c) and mass density (ρ) through the relation $G = \rho c^2$. For a quasi-incompressible medium with a Poisson ratio of $\approx$0.5, Young's modulus is expressed as $E = 3G$. However, the soft tissues are viscoelastic in nature, and the computation of elasticity and viscosity requires solving a complex model. Methods to reconstruct tissue viscoelastic properties have been proposed but are usually limited to the reconstruction of elasticity and assumption of a tissue rheology model to estimate viscosity [2], [11], [16]. A local quantification of the complex shear modulus obtained by measuring the acoustic radiation force-induced creep was proposed by Amador *et al.* [17]. These measurements need to be recorded at several different locations in the tissue. Orescanin *et al.* [18] proposed the numerical solution of Navier's wave equation for the computation of the complex shear modulus. SW dispersion as a mean to compute viscoelastic properties in liver tissues has also been explored [19]–[23]. Analytical inverse problem solutions of SW scattering from a mechanical inclusion were also proposed to compute viscoelastic properties [24]–[26]. However, an experimental geometry remained simplified in these studies and needed to be known prior. In a recent study, the geometry of the mechanical inclusion could be included in the inverse problem solution to provide viscosity (loss modulus) measures [27]. However, in the latter report, no viscosity map could be obtained; a single measurement representing the mean inclusion (and surrounding medium) viscosity as a function of frequency could be provided.

Manuscript received December 2, 2018; accepted March 28, 2019. Date of publication April 11, 2019; date of current version June 5, 2019. This work was supported in part by the Fonds de Recherche du Québec Nature et Technologies (FRQNT) under Grant PR-174387 and Grant AUDC-263591, in part by the Department of Radiology, Radio-Oncology, and Nuclear Medicine of the University of Montreal, in part by the Fonds de Recherche du Québec en Santé under Grant FRQS-34939, and in part by the Canadian Institutes of Health Research under Grant CIHR-389385. *(Corresponding author: Guy Cloutier.)*

M. Bhatt, B. Chayer, F. Destrempes, M. Gesnik, and L. Allard are with the Laboratory of Biorheology and Medical Ultrasonics, University of Montreal Hospital Research Centre, Montreal, QC H2X 0A9, Canada.

M. A. C. Moussu was with the Laboratory of Biorheology and Medical Ultrasonics, University of Montreal Hospital Research Centre, Montreal, QC H2X 0A9, Canada. She is now with the Institut Fresnel, 13397 Marseille, France.

A. Tang is with the Clinical Laboratory of Image Processing, University of Montreal Hospital Research Centre, Montreal, QC H2X 0A9, Canada, with the Institute of Biomedical Engineering, University of Montreal, Montreal, QC H3C 3J7, Canada, and also with the Department of Radiology, Radio-Oncology and Nuclear Medicine, University of Montreal, Montreal, QC H3T 1J4, Canada.

G. Cloutier is with the Laboratory of Biorheology and Medical Ultrasonics, University of Montreal Hospital Research Centre, Montreal, QC H2X 0A9, Canada, with the Institute of Biomedical Engineering, University of Montreal, Montreal, QC H3C 3J7, Canada, and also with the Department of Radiology, Radio-Oncology and Nuclear Medicine, University of Montreal, Montreal, QC H3T 1J4, Canada (e-mail: guy.cloutier@umontreal.ca).

Digital Object Identifier 10.1109/TUFFC.2019.2908550

Properties, such as shear loss modulus (G''), from which viscosity map of a tissue can be estimated, may provide more information for tissue characterization. However, tissue viscosity has not been studied much due to difficulty in an accurate computation of G'' [28]. An attempt to reconstruct viscosity was first carried out in preliminary magnetic resonance (MR) elastography studies, which indicated that tumors and fibroadenomas have a higher viscosity than typical breast tissues [29], [30]. Giannoula and Cobbold [31] and Giannoula *et al.* [32] proposed a simulation study for viscosity map reconstruction; however, no experimental US validation was performed. Girnyk *et al.* [33] studied experimental testing of a few possible algorithms for tissue viscosity and elasticity assessment but concluded that creating actual elasticity and viscosity maps required further study of tissue viscosity contribution. Ouared *et al.* [34] proposed a finite-element method-based model to obtain viscoelastic properties, but significant errors were observed in G'' computation for the cases of biases in lesion dimension and position. Schmitt *et al.* [35], [36] performed viscoelastic studies in arterial walls and blood clots and found computational challenges due to the strong dependence on model parameters. Optical methods such as an approach based on laser speckle rheology to assess tissue viscoelasticity were demonstrated by measuring the time constant of fluctuations of laser speckle intensity [37], [38]. A model-independent method for the quantitative measurement of viscoelastic parameters, proposed by Kazemirad *et al.* [39], is based on the assumption that SWs generated using an acoustic radiation force sequence travel with cylindrical wavefronts. Similar methods built on the same geometrical assumption were also developed by Budelli *et al.* [40] and others [41], [42] for quantitative viscoelastic measurements. This cylindrical wavefront model assumes a macroscopically homogeneous and isotropic propagation medium to provide a quantitative estimation of mean viscoelasticity. Reconstruction of viscosity maps was not explored in depth in our latter report to investigate complex (and heterogeneous) structures [39].

It is well known that the radiation force source generated by linear US probes is not infinitely long and does not produce perfectly cylindrical wavefronts. A shortcoming of assuming cylindrical wavefronts is that it does not model the dissipation of wave energy accurately, especially in heterogeneous media [17]. This causes imprecision in viscosity or loss modulus computation since G'' is directly related to the energy dissipated through viscous damping. Thus, such models have their own limitations for viscosity reconstruction, which may jeopardize their clinical adoption. Moreover, in many soft tissues, the wave generated by a line source does not fit the cylindrical wavefront assumption due to a direction-dependent SW velocity, which can also induce a tissue-dependent bias in attenuation. Thus, a method free from geometrical assumptions needs to be explored for improved viscosity modeling.

An important step that can lead to viscosity reconstruction in biological tissues is the accurate computation of SW attenuation and velocity. The attenuation and geometrical spreading (diffraction) of the wave generally influence the amplitude, as the wave travels through a distance. In anisotropic tissues, strong geometrical assumptions (such as cylindrical spreading of the waves) may not provide definite results. Recently, a method based on frequency-shift measurements to compute the SW attenuation was proposed by our group [43]. This method is not sensitive to wave diffraction effects (i.e., geometrical spreading of the wave energy) and presents potent accuracy. This paper utilizes the frequency-shift method to compute SW attenuation and presents an experimental validation study aiming to reconstruct the viscosity maps of irregular structures. The study demonstrates viscosity reconstruction in *in vitro* gelatin phantoms, *ex vivo* porcine liver samples, *ex vivo* fatty duck liver samples, and an *in vivo* fatty goose liver. There are very few studies that aimed to quantitatively measure the viscosity of biological tissues [29], [33], [39], [40] and few presented viscosity map reconstructions in US SW elastography. Thus, we anticipate that these results will reveal the usefulness of viscosity-based studies for soft tissues and open the window to newer perspectives in diagnostic clinical applications.

II. Methods and Materials

A. Shear Wave Propagation in a Viscoelastic Medium

SWs can be generated inside a soft tissue with conventional ultrasonic probes by relying on the focused acoustic radiation force produced by a long pushing US beam. The radiation force causes a few micrometers displacement within the tissue that propagates as a transient SW. The physical frameworks utilized for modeling SW propagation are presented in Sections II-A.1–II-A.3. The cylindrical wavefront approximation and the SW frequency-shift method are reviewed. Both approaches have been considered in the present study.

1) Cylindrical Wavefront Assumption: In an infinite, homogeneous, and isotropic viscoelastic material, Navier's equation governs the wave motion. Assuming pure SW propagation inside a soft tissue, the simplified wave equation can be written as [44]

$$\rho \frac{\partial^2 u(r,t)}{\partial t^2} = G\Delta^2 u(r,t) \tag{1}$$

where ρ is the material density, G is the complex shear modulus, and $u(r,t)$ is the transverse displacement vector in space–time (r,t).

In the case of cylindrical SW propagation, the solution to the wave equation in the frequency domain can be written as [39]

$$U(r,\omega) = a(\omega)\frac{i}{4}H_0^1(\hat{k}(\omega)r) \tag{2}$$

where r is the radial direction of the assumed cylindrical coordinate system, ω is the angular frequency, $a(\omega)$ is related to the amplitude term, H_0^1 denotes the Hankel function of the first kind of order zero, and $\hat{k}$ is the complex wavenumber.

The SW propagation can also be written in terms of displacement amplitude and phase angle as [39]

$$U(r,\omega) = ||U(r,\omega)||e^{-i\theta(U(r,\omega))} \tag{3}$$

where $||U(r,\omega)||$ is the displacement amplitude of the cylindrical SW and $\theta(U(r,\omega))$ is the phase angle. The following equation was proposed by Kazemirad *et al.* [39] and

Budelli *et al.* [40] as a measure of diffraction correction by making the cylindrical wavefront assumption:

$$\log_e(||U(r,\omega)||) = \log_e(||U_0(r,\omega)||) - r\alpha - \frac{\log_e(r)}{2} \quad (4)$$

where $U_0(r,\omega)$ is the initial displacement. With this approach, the attenuation coefficient (α) is estimated through the numerical solution (least-square fitting) of (4). The detailed description of this method can be found in [39] and [40].

However, this method has its own limitations. In particular, it assumes that acoustic pushes are being made simultaneously in a homogeneous medium, resulting in infinitely long cylindrical wavefronts. However, the radiation force generated by the linear US probes is neither infinitely long in the depth direction nor does it generates perfectly cylindrical shear wavefronts. In fact, the waves that are generated decrease in amplitude at a slower rate than purely cylindrical waves [42]. Moreover, many biological tissues are anisotropic or heterogeneous, and in such cases, the cylindrical wavefront assumption may induce a tissue-dependent bias in the attenuation coefficient computation.

2) Frequency-Shift Method: Recently, a new method considering the amplitude spectral distribution called the frequency-shift method was proposed by our group [43] to describe the SW propagation in soft tissues for use in dynamic SW elastography. This method, which is built from the analysis of the spectral properties of generated SWs, does not depend on the assumption of a cylindrical wavefront and is, in fact, free from geometrical restrictions. Briefly, if a SW has a frequency spectrum $S(f)$ at point x_0, then at a distance $x = x_0 + \Delta x$, the frequency spectrum $R(f)$ can be given as [43], [45]

$$|R(f)| = G_s(f,x) \cdot H(f,\Delta x) \cdot |S(f)| \quad (5)$$

where f is the frequency, $G_s(f,x)$ relates to the geometrical spreading of the propagating wave and $H(f,\Delta x)$ corresponds to the viscous attenuation effect on the wave amplitude. This method overcomes the geometrical spreading effects by assuming $G_s(f,x) = G_s(x)$ and considers a linear attenuation model with respect to frequency, given as

$$H(f,\Delta x) = e^{-\alpha_0 f \Delta x} \quad (6)$$

where α_0 is the linear attenuation coefficient (in units Np/m/Hz) and $\alpha = \alpha_0 \times f$ [32], [43]. The amplitude spectrum of SWs with this model is assumed to be proportional to a gamma distribution. The assessment of this hypothesis is presented in Section III-D.1. This assumption can be written as

$$|S(f)| \propto f^{k_0-1} e^{-f\beta_o} \quad (7)$$

where k_0 and β_0 are the shape and rate parameters, respectively. Thus, counting the proportionality constant, this model has three degrees of freedom. Combining (5)–(7), the frequency spectrum at location $x = x_0 + \Delta x$ can be written as

$$|R(f)| \propto f^{k_0-1} e^{-f(\beta_o + \alpha_0 \Delta x)}. \quad (8)$$

The rate parameter of (8) is $\beta(\Delta x) = \beta_o + \alpha_0 \Delta x$. As it can be observed in this equation, the linear attenuation coefficient (α_0) becomes the slope of the varying rate parameter $\beta(\Delta x)$.

At each lateral position (x_0), a nonlinear least-square algorithm (such as Levenberg–Marquardt) can be used to estimate the shape and rate parameters (k_0 and β_0) of the gamma distribution model. The curve $\beta(\Delta x)$ is then fitted to a straight line over the distance covered in the lateral direction, i.e., x_0 to $x_0 + \Delta x$. The slope of this straight line is the linear attenuation coefficient α_0. Readers are encouraged to refer to [43] for more details.

3) Estimation of the Loss Modulus: The local estimation of two parameters, namely the attenuation coefficient and the SW phase velocity, is required to compute storage and loss moduli [40]. The phase velocity (c), which is generally expressed in the form ω/k_r, can be defined as the speed of the wave propagating at a constant phase. Here, k_r is the real part of the complex wavenumber ($\hat{k}$). The phase velocity can be computed in different ways as explored in the prior literature [12], [46]–[48]. In this study, the phase velocity was computed at each position along the x-axis at a given depth by linearly fitting the phase delay of the wave field versus distance for a step-size length of 5.3 mm (15 pixels) [40]. In other words, the phase velocity (c) was estimated by measuring the phase shift $\Delta\varphi$ over a distance Δx

$$c = \omega \Delta x / \Delta\varphi. \quad (9)$$

Finally, the shear viscous or loss modulus (G'') and (dynamic) viscosity (η) were retrieved as a function of the SW speed and attenuation using [17], [39], [42]

$$G'' = 2c^2\omega^2\alpha \frac{\rho\omega c}{(c^2\alpha^2 + \omega^2)^2} \quad (10)$$

$$\text{and } \eta = \frac{G''}{\omega}. \quad (11)$$

Although the dynamic viscosity is, sometimes, defined as $\eta = G''/\omega$ [39], another common measure of viscosity in linear rheology is the shear viscous modulus or loss modulus (G''). The parameters η (in Pa.s) and G'' (in Pa) are, sometimes, used interchangeably as a measure of viscosity. Both were assessed for the animal tissue considered in the present study. Note that, in (10), the attenuation coefficient (α), which is equal to the imaginary part of the complex wavenumber ($\hat{k}$), was computed either using (4) when considering the cylindrical wavefront assumption, or using (8) when considering the frequency-shift method. Viscosity in (11) is simply brought in from the linear hypothesis of viscoelasticity (or Voigt model hypothesis) [31].

Both the cylindrical wavefront method and the frequency-shift method were used to create viscosity maps of the tissue-mimicking homogeneous phantoms.

B. Preparation of Samples

The study was performed on tissue-mimicking phantoms as well as on *ex vivo* and *in vivo* animal tissue samples.

1) Tissue-Mimicking Phantoms: Four tissue-mimicking phantoms were prepared using two basic mixtures of gelatin (Type A, #G2500, Carolina Biological Supply, Burlington, NC, USA) and Sigmacell cellulose particles with a nominal diameter of 50 μm (Type 50, #S5504, Sigma-Aldrich Chemical, St. Louis, MO, USA). Different proportions of dietary

TABLE I
WEIGHT PROPORTIONS (w/w) OF TISSUE-MIMICKING PHANTOMS' INGREDIENTS

Phantom number	Gelatin	Sigmacell cellulose	Xanthan gum	Graphite
1	5%	1.5%	0.1%	--
2	5%	1.5%	Left block = 0.6% Right block = 0.1%	--
3	5%	1.5%	Inclusion = 0.2% Surrounding = 0.5%	Inclusion = 0.1%
4	5%	1.5%	Inclusion = 0.5% Surrounding = 0.2%	Inclusion = 0.1%

xanthan gum were added (see Table I). The first phantom was homogeneous, the second was heterogeneous consisting of two different viscoelastic blocks cast side-by-side, the third one was heterogeneous with a bean-shaped inclusion of lesser viscosity than the surrounding medium, and the last one was also heterogeneous with a star-shaped inclusion of higher viscosity than the surrounding medium. The aim of preparation of such phantoms was to have varied features, such as different boundaries, shapes, or viscosities.

The stiffness was driven by the gelatin, and to study only the effect of viscosity, the gelatin concentration for all phantoms was kept the same and no other elasticity contrast was introduced. The xanthan gum was responsible for viscosity, and mixtures with more weight proportions were expected to be more viscous. Thus, only viscosity contrast was blended into heterogeneous phantoms (#2–#4). Sigmacell cellulose was used as acoustic scatterers. Graphite was added in the inclusion materials to obtain a clean visual perception of mimicking lesions to facilitate the positioning of the US probe during measurements.

The recipe to prepare the tissue-mimicking phantom material was as follows. The required percentage of gelatin and xanthan gum was dry mixed and then added to distilled water at room temperature. The solution was heated to 90 °C while smoothly stirring to gradually dissolve gelatin and xanthan gum. When the solution became clear and homogeneous, it was allowed to gradually cool down while continuously stirring, and then, the Sigmacell cellulose powder (and graphite for the inclusion material) was added at 40 °C. The solution was then allowed to return to room temperature and then cast into a rectangular box. For inclusion phantoms (#3 and #4), molds made of acrylonitrile butadiene styrene (ABS) were 3-D printed (Dimension Elite, Stratasys Inc., Eden Prairie, MN, USA), and the ABS inclusion was cast within the surrounding gel medium. The mold was removed and the inclusion was filled with the xanthan gum-based gel. For planar SW experiments (details follow), a Plexiglas (acrylic glass) plate was placed in the solution while casting [26]. The phantoms were kept in a refrigerator overnight for 16 h at a temperature of 4 °C to ensure uniform gelation. Samples were subsequently allowed to naturally return to room temperature (22 °C) prior to measurements.

2) Animal Tissue Samples: Two fresh porcine liver pieces were obtained from a grocery store to represent a normal (healthy) *ex vivo* liver tissue. Pathological fatty livers were also studied *ex vivo*. Two packaged pieces of fresh fatty duck liver samples were bought from a specialized grocery store. *In vivo* viscoelastic US measurements on a fatty goose liver (steatosis grade unknown), which was raised for foie-gras consumption, were also performed at a farmhouse. The protocol was approved by the ethical animal health care committee of the University of Montreal Hospital Research Centre. The objective was to learn whether *ex vivo* and *in vivo* fatty liver samples have similar viscous properties. This would also determine the proposed model's suitability for *in vivo* measurements.

C. Ultrasound Measurements

An acoustic radiation force beam sequence similar to SSI was implemented on a research US system (Verasonics V1, Verasonics Inc., Redmond, WA, USA) [10]. A linear array probe (ATL L7-4, Philips, Bothell, WA, USA) was used at a central frequency of 5 MHz to remotely generate SWs inside the samples. Each sequence generated three focused pushes spaced 5 mm apart inside the sample; the first push was at a depth of 2 cm. A similar sequence generated by the same setup was found well within the acceptable range of mechanical index and intensity suggested by the U.S. Food and Drug Administration for *in vivo* applications [49]. Each individual beam was focused with a pushing velocity of 40 m/s for the duration of 100 μs, with a delay of 125 μs between the consecutive pushes. The ratio of pushing velocity to SW propagation velocity, also known as the Mach number, varied between 10 and 22 for different samples depending on their mechanical properties. Immediately after generating the radiation pressure, the same US transducer was used to record plane-wave imaging radio-frequency (RF) data at a 4-kHz frame rate. The data recording step was repeated ten times in a very short time duration (less than 500 ms overall) with yet enough time for the generated SW field to completely vanish in the observed imaging domain between two successive acquisitions.

US phantom experiments were repeated for *ex vivo* porcine liver and *ex vivo* fatty duck liver samples with exactly the same procedure. The probe was positioned arbitrarily on the surface of each sample a few times, and the data were analyzed for the region where relatively lesser noisy wave fields were observed (i.e., a well-structured propagating wavefront). The same procedure was also repeated for *in vivo* measurements of a goose liver in the presence of a veterinarian performing US acquisitions. The skin of the animal around the liver area was exposed by plucking the feathers under the footprint of the US probe and covered with an acoustic gel.

Recorded RF data were beamformed using a Fourier domain method [50]. The particle velocity field was estimated from the experimental RF data using a conventional 1-D normalized cross-correlation algorithm [47]. The velocity field was

averaged over the acquired set of experiments to decrease the impact of random noise. It should be noted that SWs generated inside each sample are broadband in nature. Thus, to observe changes in properties, such as velocity, attenuation, and shear viscous or loss modulus relative to SW frequency, we also carried out planar SW experiments (with a vibrating plate). Planar SW experiments have been performed to avoid diffraction effects [39], [43].

D. Planar Shear Wave Measurements

Plane SW experiments were performed with a homogeneous phantom (similar to phantom #1) using a standard experimental setup similar to [51]. A 9 cm × 13 cm Plexiglas plate was embedded within the phantom to generate semiplanar SWs inside the sample. This plate was connected to an electronic mini shaker (type 4810, Brüel & Kjær, Nærum, Denmark), which was further connected to an arbitrary waveform generator (33250A, Agilent Technologies, Santa Clara, CA, USA) and a power amplifier (type 2706, Brüel & Kjær). This setup was capable of generating monochromatic plane SWs at any frequency of interest. Excitation signals were 10 Vpp (peak-to-peak voltage), and eight periods Blackman-windowed sinusoids were used to induce vibrations of the inserted plate. The experiment was carried out for five equidistant frequencies from 200 to 1000 Hz. The RF data of particle displacements were recorded using the same plane-wave beamforming technique as before, with a frame rate of 4 kHz for 60 ms immediately after the excitation of the plate. The same transducer (ATL L7-4, Philips, Bothell, WA, USA) was used for data acquisition.

E. Postprocessing of the Data

Since all computations were performed in the frequency domain, apodization was performed on temporal signals to smooth discontinuities at the end-points via a Tukey (tapered cosine) window. An example of apodization is shown in Fig. 1 for a temporal particle velocity field signal, which resulted in a smoother frequency spectrum. A directional filter was applied to the velocity field to discard wave reflections coming from sample boundaries/interfaces, and a simple low-pass filter eliminated aberrant noise peaks. Thus, only processing the forward propagating SW data was analyzed [52]. Cubic interpolation was applied to the computed loss modulus vector before reconstructing the viscosity images.

F. Statistical Analysis

Statistical analyses were carried out at several steps to explore further insights from this study.

1) Evaluation of Goodness of Fit: The coefficient of determination statistic, also known as the R^2-statistic, was applied to evaluate the quality of fit of the proposed gamma model to the amplitude spectrum of SWs generated by an acoustic radiation force. The R^2-statistic was computed as

$$R^2 = 1 - \frac{\sum_j ||y_j - \hat{y}_j||^2}{\sum_j ||y_j - \bar{y}||^2} \tag{12}$$

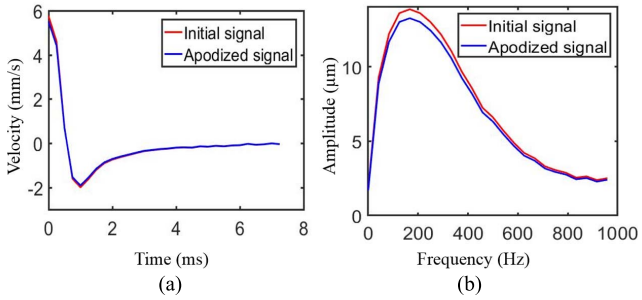

Fig. 1. Example of apodization performed on (a) temporal profile of the recorded particle velocity field along with the apodized signal (superimposed). (b) Effect of apodization as observed in the frequency domain.

where y is the measured data, $\hat{y}$ is the model predicted data, $\bar{y}$ is the mean value of the data vector y, and subscript j indicates the jth element in the data sample. The closer the R^2-statistic is to 1, the better is the model fit to the SW amplitude spectrum data. Furthermore, F-statistic scores were reported to assess R^2-statistics [53]. The F-statistic score allows inferring the p-value by looking at the table of F-distribution (in this case, with three degrees of freedom in the fitted model). As per this table, F-statistic scores were required to be greater than 8.53 for p-values to reach a statistical confidence level of 0.05 [53].

2) Variability of Acoustic Parameters: The coefficient of variation (standard deviation-to-mean ratio) was computed for SW phase velocity, SW attenuation, and viscosity near the central horizontal axis of the region of interest (ROI) for 5-mm depth in the z-direction, at each point along the x-axis (lateral position). The objective was to assess variabilities among the studied parameters along the lateral distance.

3) Fisher Criterion: The Fisher criterion (J) was used to distinguish the features inside phantom inclusions from those of its surrounding. The Fisher criterion is expressed as [54]

$$J = \frac{(\mu_2 - \mu_1)^2}{\sigma_2^2 + \sigma_1^2} \tag{13}$$

where μ and σ correspond to the mean and standard deviation of the property, and subscripts 1 and 2 correspond to medium 1 (surrounding) and medium 2 (inclusion). This parameter was used to determine which of the following three properties—SW phase velocity, SW attenuation, or viscosity—provided the best ability to distinguish the inclusion from the surrounding material, akin to a contrast-to-noise ratio (CNR). A higher score of criterion J implies a better CNR.

III. Results

A. Viscosity Reconstruction in Phantoms

An ROI of approximately 18.2 mm (lateral) × 15.9 mm (axial) was selected to reconstruct viscosity maps in all phantoms. Reconstruction maps of SW phase velocity, SW attenuation, and viscosity were computed. The ROI was chosen at least 4 mm away from the pushes to prevent reverberation artifacts [46], [55]. RF acquisitions started 0.5 ms after the pushes, and for clarity, the acoustic radiation force pushes location is marked as 0 mm in the lateral direction on B-mode

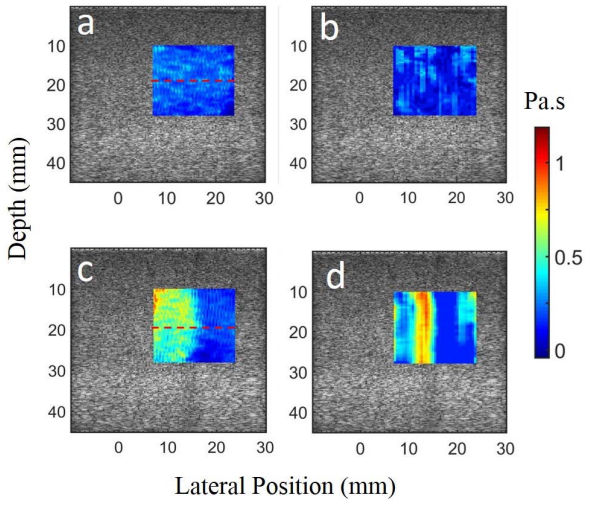

Fig. 2. Top row: viscosity reconstruction for phantom #1 using (a) proposed frequency-shift model and (b) cylindrical wavefront model. Bottom row: viscosity reconstruction for phantom #2 using (c) proposed model and (d) cylindrical wavefront model.

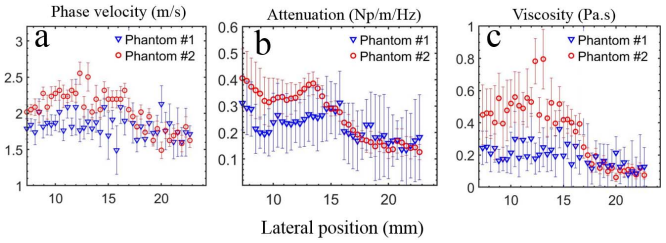

Fig. 3. (a) SW phase velocity, (b) SW attenuation, and (c) viscosity plots with respect to the wave propagation distance for phantoms #1 and #2 along the central horizontal line of the ROI shown in Fig. 2(a) and (c). Uncertainties are shown as variations in the vertical directions (mean ± SD) within the ROI for each lateral position. The frequency-shift model was used.

images. SW properties reported here (c, G'', and η) were computed at the 400-Hz SW frequency [see (9)–(11)], except for the plane-wave experiments (see Section III-C).

Fig. 2 displays the reconstructed viscosity maps for the first two phantoms. As expected, uniform maps were obtained for the homogeneous phantom #1, whatever the reconstruction method used. Phantom #2 consisted of two different viscoelastic blocks side-by-side, which is distinct in Fig. 2(c) and appears as a relatively clear boundary. For that latter phantom #2, the cylindrical wavefront assumption reconstruction method provided worse results [see Fig. 2(d)]. Note that phantom #1 and the right side block of phantom #2 were prepared in the same batch with the same materials and had the same properties.

Representative profile plots for SW phase velocity, SW attenuation, and viscosity along the central horizontal line of the ROI in phantoms #1 and #2 are shown in Fig. 3(a)–(c) for the sole purpose of clearer visualization of these properties for the proposed model. For phantom #1, the mean values of these properties in the ROI were (mean ± SD) 1.85 ± 0.21 m/s, 0.23 ± 0.11 Np/m/Hz, and 0.22 ± 0.14 Pa.s, respectively. For phantom #2, the mean values of these properties in the left side block were 2.23 ± 0.14 m/s, 0.38 ± 0.08 Np/m/Hz, and 0.57 ± 0.16 Pa.s, respectively, and the

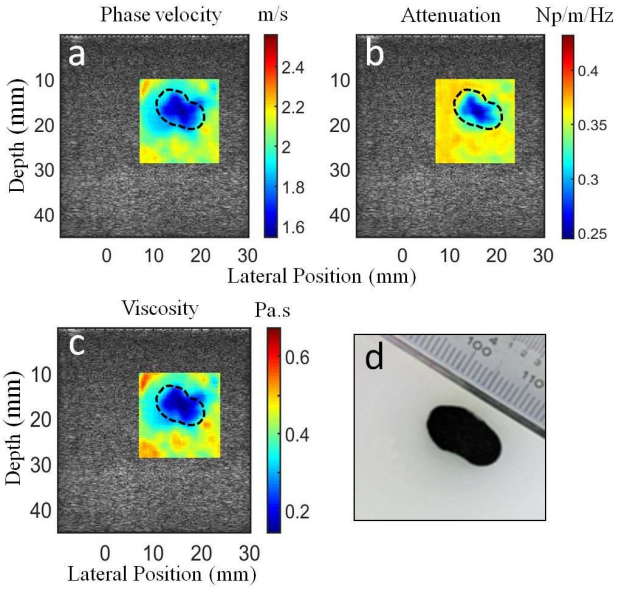

Fig. 4. Reconstruction of (a) SW phase velocity, (b) SW attenuation, and (c) viscosity. (d) Photograph of the corresponding bean-shaped phantom #3. The frequency-shift model was used.

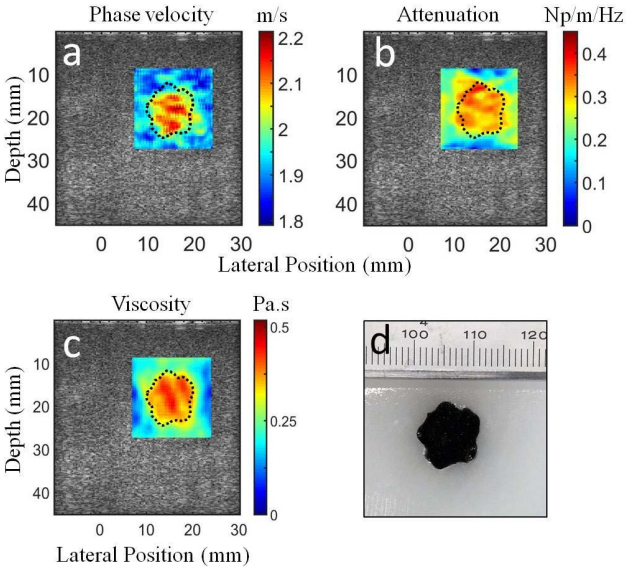

Fig. 5. Reconstruction of (a) SW phase velocity, (b) SW attenuation, and (c) viscosity. (d) Photograph of the corresponding star-shaped phantom #4. The frequency-shift model was used.

mean values in the right side block were 1.80 ± 0.13 m/s, 0.15 ± 0.05 Np/m/Hz, and 0.12 ± 0.05 Pa.s, respectively. Since the right half of phantom #2 had the same properties as phantom #1, their plots in Fig. 3 overlap in the right half zone.

The next two phantoms #3 and #4 had embedded inclusions of irregular shape. The reconstruction maps for SW phase velocity, SW attenuation, and viscosity for phantom #3 with the proposed frequency-shift model are shown in Fig. 4(a)–(c), respectively. The same results for phantom #4 are given in Fig. 5(a)–(c), respectively. In Fig. 4, the mean values of SW phase velocity, SW attenuation, and viscosity inside the inclusion were (mean ± SD) 1.68 ± 0.14 m/s, 0.29 ± 0.04 Np/m/Hz, and 0.18 ± 0.06 Pa.s, respectively, and outside the inclusion, they were

TABLE II

QUANTITATIVE VALUES (MEAN ± SD) OF THE SW PHASE VELOCITY, SW ATTENUATION, VISCOSITY, SHEAR LOSS MODULUS, AND SHEAR STORAGE MODULUS OBTAINED FOR ANIMAL LIVER SAMPLES

Tissue sample	SW phase velocity (m/s)	SW attenuation (Np/m/Hz)	Viscosity (Pa.s)	Shear loss modulus (kPa)	Shear storage modulus (kPa)
ex vivo porcine liver #1	2.12 ± 0.51	0.43 ± 0.11	0.61 ± 0.21	1.53 ± 0.62	4.85 ± 1.58
ex vivo porcine liver #2	2.0 ± 0.76	0.47 ± 0.18	0.52 ± 0.35	1.30 ± 0.88	3.95 ± 1.77
ex vivo fatty duck liver #1	3.84 ± 1.49	0.17 ± 0.06	1.28 ± 0.54	3.21 ± 1.35	14.65 ± 7.03
ex vivo fatty duck liver #2	3.71 ± 1.29	0.20 ± 0.08	1.36 ± 0.73	3.38 ± 1.46	13.83 ± 6.36
in vivo fatty goose liver	3.51 ± 1.19	0.30 ± 0.12	1.67 ± 0.70	4.18 ± 1.75	11.87 ± 4.18

2.07 ± 0.11 m/s, 0.36 ± 0.04 Np/m/Hz, and 0.44 ± 0.08 Pa.s, respectively. A photograph of the bean-shaped inclusion embedded in phantom #3 is shown in Fig. 4(d). For Fig. 5, the mean values of phase velocity, attenuation, and viscosity inside the inclusion were 2.08 ± 0.15 m/s, 0.32 ± 0.05 Np/m/Hz, and 0.39 ± 0.08 Pa.s, respectively, and outside the inclusion, these measures were 1.90 ± 0.11 m/s, 0.23 ± 0.08 Np/m/Hz, and 0.22 ± 0.07 Pa.s, respectively. A photograph of the star-shaped inclusion embedded in phantom #4 is shown in Fig. 5(d). For completeness and comparison, viscosity maps of phantoms #3 and #4 obtained with the cylindrical wavefront model assumption are given in Appendix A. As can be seen, this latter model produced inaccurate results in the case of mechanical inclusions.

B. Viscosity Computation in Animal Livers

Animal tissue samples are often anisotropic and inhomogeneous; thus, some variations in viscosity map values were expected. Representative reconstructed maps are shown in Fig. 6(a)–(c) for the *ex vivo* normal porcine liver, the *ex vivo* fatty duck liver, and the *in vivo* fatty goose liver. Fig. 6(d) shows the quantitative values of viscosity for all animal tissues studied, where it can be observed that the fatty duck liver and fatty goose liver tissues yielded higher viscosities than the porcine liver tissues. Table II lists the quantitative mean values of SW velocity, SW attenuation, and viscosity for all animal tissue samples. In addition, the shear loss modulus and the shear storage modulus are also listed.

C. Behavior of the SW Frequency on Acoustic and Viscosity Parameters

Although the validity of the frequency-shift method for SW attenuation computation was already established using

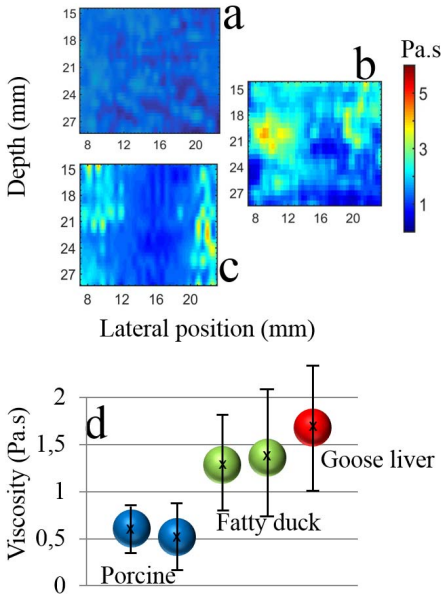

Fig. 6. Reconstruction of viscosity in (a) *ex vivo* normal porcine liver #1, (b) *ex vivo* fatty duck liver #1, and (c) *in vivo* fatty goose liver. (d) Mean (± SD) quantitative values of viscosity for the examined animal tissues. The frequency-shift model was used.

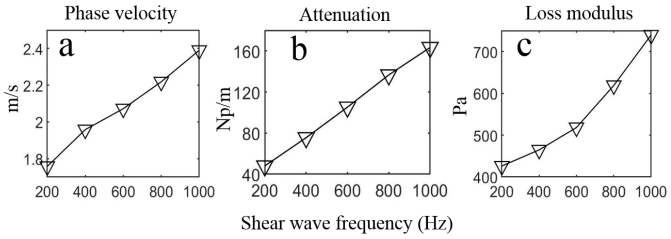

Fig. 7. Changes in properties of (a) SW phase velocity, (b) SW attenuation, and (c) shear viscous or loss modulus (G'') relative to the SW frequency. Planar SW experiments were conducted, and the frequency-shift model was used.

plane-wave experiments [43], we repeated those experiments to observe the behavior of the SW frequency distribution on viscosity modulus. Experiments were performed as discussed in Section II-D using a homogeneous phantom. Fig. 7 shows the plots of the SW phase velocity, SW attenuation (in Np/m units), and shear viscous or loss modulus (G'') relative to the SW frequency. The three properties were observed to be proportional to the SW frequency.

D. Results from Statistical Analyses

1) Validation of the Proposed Model Fit: The coefficient of determination statistic evaluated the quality of the gamma model fit for a representative heterogeneous sample (phantom #4). The test was performed at several points located along the red horizontal line shown in Fig. 8(a). The goodness-of-fit statistic (R^2) and the F-statistic scores are provided in Table III for ten such equidistant points. As seen, the SW amplitude spectrum at 9 out of 10 points had model fit match between 92% and 98%, and the corresponding F-statistics were greater than 8.53. An illustration of the amplitude spectrum and its model fit at one of the points is shown in Fig. 8(b). The test failed at the 11.87-mm location, which is near the boundary

TABLE III

R^2- AND F-STATISTICS FROM THE COEFFICIENT OF DETERMINATION TEST TO ASSESS THE QUALITY OF THE MODEL FIT TO THE AMPLITUDE SPECTRUM OF TIME SIGNALS OF PROPAGATING SWS AT VARIOUS LATERAL POSITIONS IN PHANTOM #4. THESE LOCATIONS ARE SITUATED EQUIDISTANTLY ALONG THE RED HORIZONTAL LINE SHOWN IN FIG. 8(A)

Lateral position (mm)	5.62	7.18	8.75	10.31	11.87	13.43	15.0	16.56	18.12	19.68
R^2 statistic	0.94	0.92	0.95	0.96	0.78	0.98	0.93	0.97	0.96	0.97
F statistic	15.22	11.33	20.03	25.32	3.45	41.89	12.56	29.62	26.73	35.02

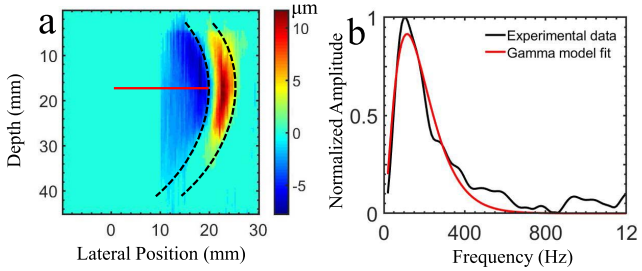

Fig. 8. (a) Snapshot of the forward propagating SW's displacement map in phantom #4. The black dashed lines are drawn to outline the shape of the propagating wavefront. The acoustic pushes were made at a 0-mm lateral position, and the goodness-of-fit test was evaluated along the red horizontal line. (b) Representative amplitude spectrum of the time signal of the forward propagating wave recorded during a positive vibration cycle, and its gamma fit.

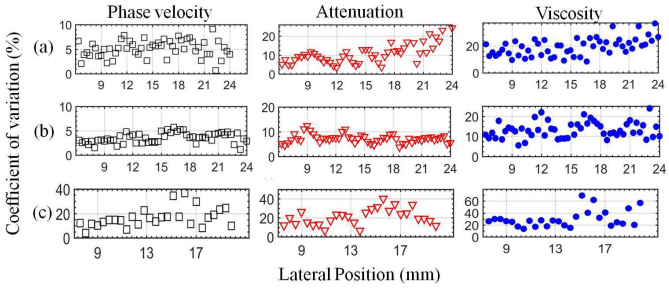

Fig. 9. Coefficient of variation plots of the SW phase velocity, SW attenuation, and viscosity computed using the frequency-shift model for (a) phantom #2, (b) phantom #4, and (c) *ex vivo* porcine liver #2.

of the inclusion, as can be noticed from Fig. 5. The goodness of fit for homogeneous samples including animal tissues was already provided in [43]; thus, we only present the results for one heterogeneous sample here.

2) Variability of the Studied Parameters Along the Lateral Distance: Fig. 9 shows the coefficients of variation for the SW phase velocity, SW attenuation, and viscosity in the ROI for three representative samples (phantoms #2 and #4, and porcine liver #2). Results from all the experiments are summarized in Table IV for two sets of lateral distances from the acoustic radiation force pushing axis at positions: 1) less than 13 mm and 2) beyond 13 mm. The variability was higher at farther distances.

3) Contrast Between the Inclusion and Surrounding Material: Probability density functions of SW phase velocity, SW attenuation, and viscosity are shown in Fig. 10, where two color-coded curves correspond to properties within the inclusion (red color) or surrounding region (blue color). The intersection area under the two curves represents the percentage of misclassification error. Misclassification may mean that a pixel inside the inclusion region is classified as outside the inclusion (type-1) or vice versa (type-2). The threshold of classification was set at the intersection point of the two probability density function curves, and in Fig. 10, it is divided by the black dashed line in each plot. For phantom #3, these type-1 and type-2 misclassifications were 23.3% and 13.8% for the phase velocity map, 24.9% and 11.4% for the attenuation map, and 19.6% and 13.2% for the viscosity map, respectively. Similarly, for phantom #4, the type-1 and type-2 misclassifications were 37.9% and 3.7% for the phase velocity map, 6.1% and 13.9% for the attenuation map, and 6.1% and 8.3% for the viscosity map, respectively.

The Fisher criterion scores for these three properties for phantoms #3 and #4 are listed in Table V. The highest score was observed for viscosity for both phantoms, meaning that viscosity was the best discriminator between the inclusion and the surrounding medium.

TABLE IV

MAXIMUM COEFFICIENTS OF VARIATION (%) OBSERVED FOR THE SW PHASE VELOCITY, SW ATTENUATION, AND VISCOSITY IN PHANTOMS AND ANIMAL TISSUE EXPERIMENTS. THE TWO COLUMNS UNDER EACH QUANTITY REPRESENT THE LATERAL DISTANCES (A) LESS THAN 13 mm AND (B) BEYOND 13 mm

Sample	Maximum coefficient of variation (%)					
	Phase velocity		Attenuation		Viscosity	
	a	b	a	b	a	b
Phantom #1	5	8	27	32	27	38
Phantom #2	8	10	12	26	26	36
Phantom #3	10	12	9	18	12	19
Phantom #4	5	6	13	10	22	24
ex vivo porcine liver #1	35	55	37	52	53	114
ex vivo porcine liver #2	22	37	26	41	19	69
ex vivo fatty duck liver #1	31	48	29	45	51	72
ex vivo fatty duck liver #2	37	42	26	48	36	74
in vivo fatty goose liver #1	13	26	30	40	27	61

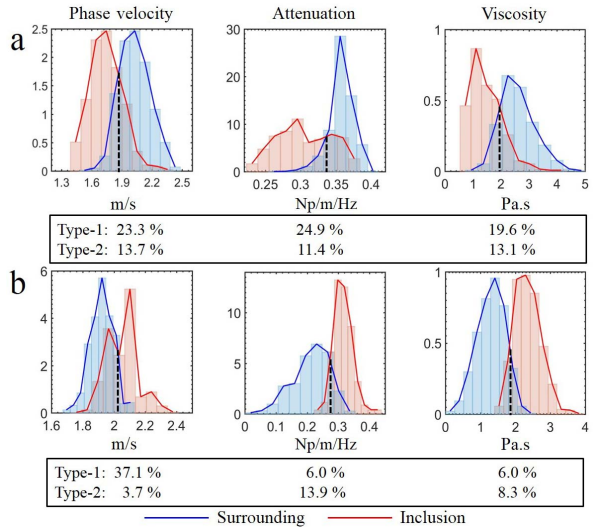

Fig. 10. (a) Probability density functions for the SW phase velocity, SW attenuation, and viscosity for phantom #3. The type-1 and type-2 misclassification errors, which are the intersection areas on each side of the black dashed line, are indicated for each plot. (b) Similar plots drawn for phantom #4.

TABLE V

FISHER (J) CRITERION FOR THE SW PHASE VELOCITY, SW ATTENUATION, AND VISCOSITY FOR PHANTOMS #3 AND #4

Property	Phantom #3	Phantom #4
SW phase velocity	1.64	1.30
SW attenuation	1.52	1.81
Viscosity	**1.75**	**2.96**

IV. DISCUSSION

In this paper, we presented a wavefront's geometry-independent physical framework based on SW frequency-shift computations that can be applied for the reconstruction of viscosity maps. The experimental validation was performed using several samples, including *ex vivo* and *in vivo* animal liver acquisitions.

A. Observations From Experimental Results

1) Phantom Experiments: Viscosity reconstruction was performed for phantoms #1 and #2 using both the cylindrical wavefront assumption method and the frequency-shift method. It could be observed from Fig. 2 that both methods provided a similar reconstruction of viscosity for the homogeneous phantom. On the other hand, change in the medium properties near the interface of two gel blocks in phantom #2 disrupted the cylindrical wavefront assumption and the effects were perceptible in Fig. 2(d). However, it should be noted that the cylindrical wavefront model was developed assuming a homogeneous medium [39], [40], and such reconstructions in heterogeneous media were expected to be prone to artifacts and errors. Viscosity computations with the proposed frequency-shift method are based on two parameters of the model—the SW phase velocity and the SW attenuation—and Fig. 3 suggests that variations in viscosity may be more strongly linked to variations in phase velocity. As it can be observed, the profile plots in Fig. 3(a) and (c) follow the same pattern.

The second set of experiments with phantoms #3 and #4 aimed at showing the method's ability to reconstruct maps in irregular shape inclusions. The mechanical inclusion in phantom #3 was less viscous than its surrounding, while the inclusion in phantom #4 was more viscous than the surrounding medium (see Table I). Since insonified media were heterogeneous, the cylindrical wavefront assumption method was no longer valid, and the results pertaining to only the frequency-shift method were presented. It could be observed from Figs. 4 and 5 that the viscosity was able to map the inclusion most systematically, an observation that was also supported by statistical analyses. Finally, these results make a point that viscosity can be used as a distinguishing property when the elasticity contrast between a medium and its surrounding is not sufficient. For completeness, this comparison is presented in Appendix B where the normalized maps of both elasticity and viscosity for phantom #4 are presented.

Clinical applications of SW elastography often display the images of SW group velocity. In soft tissues, the group velocity is significantly higher than the phase velocity, typically by a factor of 1.1–1.2 or higher [56]. Interpretation of tissue stiffness is conventionally based on the assumption of purely elastic materials. However, phantoms presented here (#2–#4) provide an opportunity to compare the group velocity values when the viscosity component is varying, while the elasticity component is fixed. Thus, we also report the SW group velocity, calculated from the time-to-peak method [57] for the averaged tissue velocity field in the z-direction for a 5-mm depth, to provide this comparison. The group velocity in the less viscous part of phantoms #2–#4 were 2.92 ± 0.05, 3.48 ± 0.08, and 3.32 ± 0.18 m/s, respectively. The group velocity in the more viscous part of phantoms #2–#4 were 3.94 ± 0.34, 3.48 ± 0.08, and 3.55 ± 0.16 m/s, respectively. This trend suggests that the SW group velocity also increases with the increase in viscosity.

2) Animal Tissue Experiments: The viscosity computation in animal tissues was carried out with twofold objectives: (1) to compare healthy liver tissues versus fatty liver tissues and (2) to compare *ex vivo* versus *in vivo* fatty liver tissues. Tissue samples from both porcine livers (healthy) resulted in approximately the same viscosity. Viscosity values of *ex vivo* duck livers and *in vivo* goose liver were also observed to be in the same range while being considerably higher than porcine liver samples. Tabaru *et al.* [58] studied the mechanical properties of foie-gras (fatty duck liver) and porcine livers, reporting Young's moduli of foie-gras (9.0–9.7 kPa) significantly higher compared with porcine livers (1.2–1.3 kPa). The latter study did not report the viscosity values. Thus, we make an observation from our experiments that fatty liver tissues have a higher viscosity than normal porcine livers. Similar trends were observed for the other two properties mentioned in Table II, i.e., the shear loss modulus and the shear storage modulus of these samples.

The comparison between the *ex vivo* fatty duck and *in vivo* fatty goose liver results revealed a slight increase in

SW attenuation *in vivo*. We did not have histology results of the goose liver to grade the steatosis stage, but it was raised for foie-gras consumption. The viscosity of these liver samples remained in the range between 1.28 $\pm$ 0.54 and 1.67 $\pm$ 0.70 Pa.s in our experiments. Finally, although *ex vivo* and *in vivo* measurements were carried out with different animal species, the scope of characterizing porcine versus duck versus goose was not covered due to the small sample size. The main objective of animal tissue experiments was to provide general trends on viscosity in healthy and fatty liver tissues and to provide a proof-of-concept of the proposed viscoelasticity imaging method.

Excessive mobilization of body fat reserves causes fatty liver. Furthermore, an increase in triglyceride content results in an increase in hepatic fat. The presence of lipids, such as cholesterol esters and triglycerides in large amounts, may also cause an increase in viscosity of fatty livers. The biochemical changes in the fatty liver have been well reported, and interested readers can refer to [59]–[61].

In biological tissues, high-frequency components of SWs dissipate rapidly with distance [39], [43]. Bernard *et al.* [43] noted that for SW propagation across the tissue fibers, a gamma fit of the amplitude spectrum is strongly dominated by noise at more than 12-mm distance away from the push location. Higher frequencies get attenuated more in biological tissues, which may cause reduced signal-to-noise ratios. Thus, the reconstruction of viscosity at higher SW frequencies may result in lower CNR. In this study, the reported reconstruction results were computed at 400 Hz since it was neither too low nor too high a frequency for our experiments. The full width at half maximum (FWHM) spectral width among the samples was observed to be mainly varying between 50 and 600 Hz. The phase velocity and the shear loss modulus are frequency-dependent parameters, and their behavior relative to frequency was shown in Fig. 7. The selection of the SW frequency certainly can affect the reconstruction quality or CNR, and this can be a wider scope of future study directions.

B. Planar Shear Wave Experiments

The acoustic radiation force experiments generated broadband SWs constituting of multiple frequencies. For planar SW experiments, the SW frequency was varied between 200 and 1000 Hz to provide a detailed spectroscopic characterization. The attenuation (in Np/m) increased with frequency, and these results were similar to those reported by Bernard *et al.* [43].

C. Insights From Statistical Analyses

1) Efficiency of the Proposed Model Fit: The displacement snapshot shown in Fig. 8(a) showed that the shear wavefront may not follow a particular geometry in nonhomogeneous media. This justified the use of a viscoelasticity model independent of the wavefront geometry as the frequency-shift method. The goodness-of-fit values given in Table III confirmed that the model [see Fig. 8(b)] was suitable to fit the SW amplitude spectrum in 9 out of 10 cases. The one exception occurred at 11.87-mm lateral position when the R^2 statistic was relatively lower, which was near the boundary of the inclusion. This suggests that the model-fit may be prone to errors near the boundary of an inclusion, i.e., when the wavefront moves from one medium to another.

2) Variability of Shear Wave Parameters: The coefficients of variation were observed to be increasing with lateral distance. Bernard *et al.* [43] also noted that 11 mm away from the acoustic radiation force pushing axis, the peak frequency estimation became inaccurate due to noise domination. One should also be careful while interpreting higher coefficients of variation in Table IV. For example, observations from Fig. 9 suggest that variabilities in phantoms before the 13-mm lateral distance mark were often lesser than 5% for SW phase velocity, lesser than 10% for SW attenuation, and lesser than 20% for viscosity computations. Similarly, variabilities in animal tissue samples were often lesser than 20% for SW phase velocity and attenuation, and lesser than 40% for viscosity computations. Beyond the 13-mm lateral distance mark, variations were more prominent. Thus, we observed that beyond the 13-mm distance from the pushing axis, computations were dominated by noise in viscous tissues for the particular experimental conditions described in this work.

3) Errors in Boundary Mapping: For phantoms with embedded inclusions, probability density functions and Fisher criterion were computed to assess the ability of viscosity maps to provide a contrast in mapping inclusion boundaries. As it was observed from the probability density function plots of Fig. 10 (through the area under intersection), there were unavoidable chances of misclassification. The reconstruction results and the probability density functions of the less viscous inclusion case (phantom #3) suggest more such errors in mapping borders. A possible explanation is that the wave field gets trapped inside a softer inclusion and makes multiple reflections on the sides, and thus, the inversion becomes more challenging. The silver lining is that the Fisher criterion score was the highest for viscosity when compared with other properties, implying that viscosity maps hold the promise to provide more accurate shape recovery.

D. Future Perspectives, Scope, and Limitations

Contrary to the assumption made in the cylindrical wavefront model (Section II-A1), the SW propagation medium (i.e., samples under investigation) cannot be considered infinite. As a result, unwanted reflections from the boundary walls are likely to occur. Furthermore, in heterogeneous phantoms, interfaces (planar ones or inclusion) are also responsible for wave reflections. This may cause artifacts in SW temporal signal shapes and affect reconstruction performance.

An important observation from this study was that a model based on a particular wavefront geometry is likely to be inaccurate for viscosity or loss modulus computations in heterogeneous samples. Most soft tissues are anisotropic, heterogeneous, or of irregular shapes, and thus, demand is for a method which would be free from geometrical assumptions. The frequency-shift method, which was first used for SW attenuation computation by our group, was shown to be advantageous for viscosity map reconstructions. Furthermore, in cases where elasticity contrast is not strong enough, viscosity could become a discriminating diagnostic feature. Moreover, the accurate computation of the

complex shear modulus can also be a direct application of the proposed model.

As it was stated in the beginning of this article, viscosity can provide a better discrimination of malignant versus benign tissues [29], [30]. Likewise, successful prognosis and management of chronic viral hepatitis require early diagnosis and effective noninvasive methods for assessing liver fibrosis. Liver elasticity may depend upon the factors other than fibrosis, such as edema, inflammation, extrahepatic cholestasis, and congestion [55], [62]; in such cases, integration of viscosity information could provide an effective adjunctive tool for quantifying liver diseases. The proof-of-concept results of the current study suggest that the proposed reconstruction method may have promising benefits, mainly for detecting the anatomy with low elasticity contrast and mapping lesion boundaries.

Finally, the potential limitation of this method is the influence of noise that affects the reconstruction performance. RF data are often corrupted with measurement noise, which may result in strong artifacts in many *in vivo* experiments. Improvement in the signal-to-noise ratio of the measured wave-field data using techniques, such as coherent plane-wave compounding [63], could significantly enhance the results. Sources of errors include, but are not limited to, motion artifacts during the US scan, the presence of air bubbles *ex vivo*, anisotropic anatomy, and upper harmonics generated inside the tissue due to nonlinear properties. More analyses to investigate the noise effects may open further possibilities.

V. Conclusion

Reconstruction of viscosity in biological tissues can provide more information during an early screening of diseases in soft tissues, like liver, breast, or brain. In this study, successful reconstructions of viscosity maps in phantoms with inclusions were presented. The method is independent of any assumption on the wavefront geometry in the investigated tissue. The proposed model holds promise for cases when the elasticity contrast may not be sufficient, and thus, added information coming from viscosity maps could be critical. Viscosity computations were also performed in animal tissues, and it was observed that the *ex vivo* fatty duck liver and *in vivo* fatty goose liver samples were more viscous than the healthy *ex vivo* porcine liver samples. We anticipate that viscosity information may provide several applications in medical diagnosis, such as the staging of fatty liver disease, the characterization of breast cancers, the assessment of brain tissues, or the rheological assessment of blood clots.

Appendix A

The viscosity reconstruction results for the mechanical inclusion phantoms #3 and #4 using the cylindrical wavefront assumption method (Section II-A1) are presented here. This method assumes that the generated SWs have cylindrical wavefronts in a homogeneous medium. However, such an assumption becomes invalid in heterogeneous media, and if this method is used, it provides inaccurate results. Fig. 11 shows such inaccuracy in the viscosity maps of phantoms #3 and #4 reconstructed using the cylindrical wavefront assumption method.

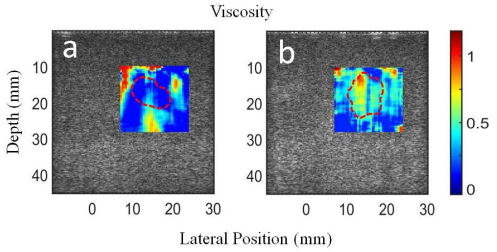

Fig. 11. Reconstruction of viscosity maps using the cylindrical wavefront assumption method in phantoms (a) #3 and (b) #4 including mechanical inclusions. As seen, both the bean- and star-shaped inclusions could not be reconstructed correctly. Viscosity maps shown here are normalized between 0 and 1 for clarity.

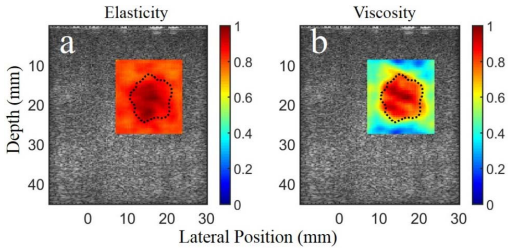

Fig. 12. Reconstruction of normalized (a) elasticity and (b) viscosity for phantom #4. The color scale on both figures is kept in the range 0–1 to compare the distinction ability of both properties.

Appendix B

The aim of this appendix was to compare the contrast ability of elasticity and viscosity maps. As an example, we compared the normalized viscoelasticity maps of phantom #4, where the inclusion was more viscous than the surrounding gel. Note that this phantom was prepared in such a way that the elasticity contrast was lesser between the inclusion and the surrounding medium, and the viscosity contrast was higher. The normalized maps for both elasticity and viscosity are shown in Fig. 12. The elasticity refers to shear elastic modulus (G') and was computed as in [39]

$$G' = \rho\omega^2 c^2 \frac{\omega^2 - c^2\alpha^2}{(\omega^2 + c^2\alpha^2)^2}. \tag{B.1}$$

The Fisher criterion score (J) was 1.04 for the elasticity map and 2.96 for the viscosity. From Fig. 12, it is clear that the viscosity map may provide more information in the case where the elasticity does not have enough contrast. Furthermore, coupled maps of elasticity and viscosity may turn out to be far-reaching for diagnostic and therapeutic applications.

Acknowledgment

The authors would like to thank F. Ouellet and Dr. A. Louvet for their assistance during goose liver data acquisitions and Dr. S. Bernard for initial discussions on this work.

References

[1] K. Nightingale, S. McAleavey, and G. Trahey, "Shear-wave generation using acoustic radiation force: *in vivo* and *ex vivo* results," *Ultrasound Med. Biol.*, vol. 29, no. 12, pp. 1715–1723, 2003.

[2] S. Chen *et al.*, "Assessment of liver viscoelasticity by using shear waves induced by ultrasound radiation force," *Radiology*, vol. 266, no. 3, pp. 964–970, Mar. 2013.

[3] J. L. Gennisson, T. Deffieux, M. Fink, and M. Tanter, "Ultrasound elastography: Principles and techniques," *Diagnostic Interventional Imag.*, vol. 94, no. 5, pp. 487–495, 2013.

[4] M. M. Doyley and K. J. Parker, "Elastography: General principles and clincial applications," *Ultrasound Clin.*, vol. 9, no. 1, pp. 1–11, 2014.

[5] A. Tang, G. Cloutier, N. M. Szeverenyi, and C. B. Sirlin, "Ultrasound elastography and MR elastography for assessing liver fibrosis—Part 1: Principles and techniques," *Amer. J. Roentgenol.*, vol. 205, no. 1, pp. 22–32, 2015.

[6] A. Tang, G. Cloutier, N. M. Szeverenyi, and C. B. Sirlin, "Ultrasound elastography and MR elastography for assessing liver fibrosis—Part 2: Diagnostic performance, confounders, and future directions," *Amer. J. Roentgenology*, vol. 205, no. 1, pp. 33–40, 2015.

[7] K. Nightingale, M. S. Soo, R. Nightingale, and G. Trahey, "Acoustic radiation force impulse imaging: *In vivo* demonstration of clinical feasibility," *Ultrasound Med. Biol.*, vol. 28, no. 2, pp. 227–235, 2002.

[8] K. Nightingale, "Acoustic radiation force impulse (ARFI) imaging: A review," *Current. Med. Imag. Rev.*, vol. 7, no. 4, pp. 328–339, Nov. 2011.

[9] M. Friedrich-Rust *et al.*, "Liver fibrosis in viral hepatitis: Noninvasive assessment with acoustic radiation force impulse imaging versus transient elastography," *Radiology*, vol. 252, no. 2, pp. 595–604, 2009.

[10] J. Bercoff, M. Tanter, and M. Fink, "Supersonic shear imaging: A new technique for soft tissue elasticity mapping," *IEEE Trans. Ultrason., Ferroelectr., Freq. Control*, vol. 51, no. 4, pp. 396–409, Apr. 2004.

[11] M. Muller, J. L. Gennisson, T. Deffieux, M. Tanter, and M. Fink, "Quantitative viscoelasticity mapping of human liver using supersonic shear imaging: Preliminary *in vivo* feasability study," *Ultrasound Med. Biol.*, vol. 35, no. 2, pp. 219–229, 2009.

[12] M. Tanter *et al.*, "Quantitative assessment of breast lesion viscoelasticity: initial clinical results using supersonic shear imaging," *Ultrasound Med. Biol.*, vol. 34, no. 9, pp. 1373–1386, 2008.

[13] C. Cassinotto *et al.*, "Liver stiffness in nonalcoholic fatty liver disease: A comparison of supersonic shear imaging, FibroScan, and ARFI with liver biopsy," *Hepatology*, vol. 63, no. 6, pp. 1817–1827, 2016.

[14] W. A. Berg *et al.*, "Shear-wave elastography improves the specificity of breast us: The be1 multinational study of 939 masses," *Radiology*, vol. 262, no. 2, pp. 435–449, 2012.

[15] D. Cosgrove *et al.*, "EFSUMB guidelines and recommendations on the clinical use of ultrasound elastography—Part 2: Clinical applications," *Ultraschall Med*, vol. 34, no. 3, pp. 238–253, 2013.

[16] S. Chen, M. Fatemi, and J. F. Greenleaf, "Quantifying elasticity and viscosity from measurement of shear wave speed dispersion," *J. Acoust. Soc. Amer.*, vol. 115, no. 6, pp. 2781–2785, Jun. 2004.

[17] C. Amador, M. W. Urban, S. Chen, and J. F. Greenleaf, "Loss tangent and complex modulus estimated by acoustic radiation force creep and shear wave dispersion," *Phys. Med. Biol.*, vol. 57, no. 5, pp. 1263–1282, 2012.

[18] M. Orescanin, Y. Wang, and M. F. Insana, "3-D FDTD simulation of shear waves for evaluation of complex modulus imaging," *IEEE Trans. Ultrason., Ferroelectr., Freq. Control*, vol. 58, no. 2, pp. 389–398, Feb. 2011.

[19] M. Orescanin, M. A. Qayyum, K. S. Toohey, and M. F. Insana, "Dispersion and shear modulus measurements of porcine liver," *Ultrason. Imag.*, vol. 32, no. 4, pp. 255–266, 2010.

[20] K. J. Parker, A. Partin, and D. J. Rubens, "What do we know about shear wave dispersion in normal and steatotic livers?" *Ultrasound Med. Biol.*, vol. 41, no. 5, pp. 1481–1487, 2015.

[21] E. Bavu *et al.*, "Noninvasive *in vivo* liver fibrosis evaluation using supersonic shear imaging: A clinical study on 113 hepatitis C virus patients," *Ultrasound Med. Biol.*, vol. 37, no. 9, pp. 1361–1373, 2011.

[22] T. Deffieux *et al.*, "Investigating liver stiffness and viscosity for fibrosis, steatosis and activity staging using shear wave elastography," *J. Hepatol.*, vol. 62, no. 2, pp. 317–324, 2015.

[23] C. T. Barry *et al.*, "Shear wave dispersion measures liver steatosis," *Ultrasound Med. Biol.*, vol. 38, no. 2, pp. 175–182, 2012.

[24] A. Hadj-Henni, C. Schmitt, and G. Cloutier, "Shear wave induced resonance elastography of soft heterogeneous media," *J. Biomech.*, vol. 43, no. 8, pp. 1488–1493, 2010.

[25] E. Montagnon, A. Hadj-Henni, C. Schmitt, and G. Cloutier, "Rheological assessment of a polymeric spherical structure using a three-dimensional shear wave scattering model in dynamic spectroscopy elastography," *IEEE Trans. Ultrason., Ferroelectr., Freq. Control*, vol. 61, no. 2, pp. 277–287, Feb. 2014.

[26] M. Bhatt, E. Montagnon, F. Destrempes, B. Chayer, S. Kazemirad, and G. Cloutier, "Acoustic radiation force induced resonance elastography of coagulating blood: Theoretical viscoelasticity modeling and *ex vivo* experimentation," *Phys. Med. Biol.*, vol. 63, no. 6, 2018, Art. no. 065018.

[27] S. Bernard and G. Cloutier, "Forward and inverse viscoelastic wave scattering by irregular inclusions for shear wave elastography," *J. Acoust. Soc. Amer.*, vol. 142, no. 4, pp. 2346–2364, 2017.

[28] M. M. Doyley, "Model-based elastography: A survey of approaches to the inverse elasticity problem," *Phys. Med. Biol.*, vol. 57, no. 3, pp. R35–R73, 2012.

[29] R. Sinkus *et al.*, "Imaging anisotropic and viscous properties of breast tissue by magnetic resonance-elastography," *Magn. Reson. Med.*, vol. 53, no. 2, pp. 372–387, Feb. 2005.

[30] A. Baghani, S. Salcudean, M. Honarvar, R. S. Sahebjavaher, R. Rohling, and R. Sinkus, "Travelling wave expansion: A model fitting approach to the inverse problem of elasticity reconstruction," *IEEE Trans. Med. Imag.*, vol. 30, no. 8, pp. 1555–1565, Aug. 2011.

[31] A. Giannoula and R. S. C. Cobbold, "Mapping the local shear modulus and viscosity using a transient finite-amplitude modulated radiation force," *Ultrasonics*, vol. 51, no. 3, pp. 340–351, 2011.

[32] A. Giannoula, R. Cobbold, and A. Bezerianos, "Reconstructing 3-D maps of the local viscoelastic properties using a finite-amplitude modulated radiation force," *Ultrasonics*, vol. 54, no. 2, pp. 563–575, 2014.

[33] S. Girnyk, A. Barannik, E. Barannik, V. Tovstiak, A. Marusenko, and V. Volokhov, "The estimation of elasticity and viscosity of soft tissues *in vitro* using the data of remote acoustic palpation," *Ultrasound Med. Biol.*, vol. 32, no. 2, pp. 211–219, 2006.

[34] A. Ouared, S. Kazemirad, E. Montagnon, and G. Cloutier, "Ultrasound viscoelasticity assessment using an adaptive torsional shear wave propagation method," *Med. Phys.*, vol. 43, no. 4, pp. 1603–1614, 2016.

[35] C. Schmitt, A. Hadj-Henni, and G. Cloutier, "Ultrasound dynamic microelastography applied to the viscoelastic characterization of soft tissues and arterial walls," *Ultrasound Med. Biol.*, vol. 36, no. 9, pp. 1492–1503, 2010.

[36] C. Schmitt, A. Hadj-Henni, and G. Cloutier, "Characterization of blood clot viscoelasticity by dynamic ultrasound elastography and modeling of the rheological behavior," *J. Biomech.*, vol. 44, no. 4, pp. 622–629, 2011.

[37] Z. Hajjarian and S. K. Nadkarni, "Evaluating the viscoelastic properties of tissue from laser speckle fluctuations," *Sci. Rep.*, vol. 2, Mar. 2012, Art. no. 316.

[38] X. Chen, Y. Wang, J. Lu, and P. Li, "Simultaneous viscosity and elasticity measurement using laser speckle contrast imaging," *Opt. Lett.*, vol. 43, no. 7, pp. 1582–1585, 2018.

[39] S. Kazemirad, S. Bernard, S. Hybois, A. Tang, and G. Cloutier, "Ultrasound shear wave viscoelastography: Model-independent quantification of the complex shear modulus," *IEEE Trans. Ultrason., Ferroelectr., Freq. Control*, vol. 63, no. 9, pp. 1399–1408, Sep. 2016.

[40] E. Budelli *et al.*, "A diffraction correction for storage and loss moduli imaging using radiation force based elastography," *Phys. Med. Biol.*, vol. 62, no. 1, pp. 91–106, 2017.

[41] I. Z. Nenadic *et al.*, "Application of attenuation measuring ultrasound shearwave elastography in 8 post-transplant liver patients," in *Proc. IEEE Int. Ultrason. Symp. (IUS)*, Chicago, IL, USA, Sep. 2014, pp. 987–990.

[42] N. C. Rouze, M. L. Palmeri, and K. R. Nightingale, "An analytic, Fourier domain description of shear wave propagation in a viscoelastic medium using asymmetric Gaussian sources," *J. Acoust. Soc. Amer.*, vol. 138, no. 2, pp. 1012–1022, 2015.

[43] S. Bernard, S. Kazemirad, and G. Cloutier, "A frequency-shift method to measure shear-wave attenuation in soft tissues," *IEEE Trans. Ultrason., Ferroelectr., Freq. Control*, vol. 64, no. 3, pp. 514–524, Mar. 2017.

[44] J. Achenbach, *Wave Propagation in Elastic Solids*. Amsterdam, The Netherlands: North Holland, 1973.

[45] Y. Quan and J. M. Harris, "Seismic attenuation tomography using the frequency shift method," *Proc. Geophys.*, vol. 62, no. 3, pp. 895–905, May 1997.

[46] T. Deffieux, G. Montaldo, M. L. Tanter, and M. Fink, "Shear wave spectroscopy for *in vivo* quantification of human soft tissues viscoelasticity," *IEEE Trans. Med. Imag.*, vol. 28, no. 3, pp. 313–322, Mar. 2009.

[47] J. Luo and E. Konofagou, "A fast normalized cross-correlation calculation method for motion estimation," *IEEE Trans. Ultrason., Ferroelectr., Freq. Control*, vol. 57, no. 6, pp. 1347–1357, Jun. 2010.
[48] A. J. Engel and G. R. Bashford, "A new method for shear wave speed estimation in shear wave elastography," *IEEE Trans. Ultrason., Ferroelectr., Freq. Control*, vol. 62, no. 12, pp. 2106–2114, Dec. 2015.
[49] A. Ouared, E. Montagnon, S. Kazemirad, L. Gaboury, A. Robidoux, and G. Cloutier, "Frequency adaptation for enhanced radiation force amplitude in dynamic elastography," *IEEE Trans. Ultrason., Ferroelectr., Freq. Control*, vol. 62, no. 8, pp. 1453–1466, Aug. 2015.
[50] D. Garcia, L. Le Tarnec, S. Muth, E. Montagnon, J. Porée, and G. Cloutier, "Stolt's f-k migration for plane wave ultrasound imaging," *IEEE Trans. Ultrason., Ferroelectr., Freq. Control*, vol. 60, no. 9, pp. 1853–1867, Sep. 2013.
[51] S. Catheline *et al.*, "Measurement of viscoelastic properties of homogeneous soft solid using transient elastography: An inverse problem approach," *J. Acoust. Soc. Amer.*, vol. 116, no. 6, pp. 3734–3741, Dec. 2004.
[52] T. Deffieux, J.-L. Gennisson, J. Bercoff, and M. Tanter, "On the effects of reflected waves in transient shear wave elastography," *IEEE Trans. Ultrason., Ferroelectr., Freq. Control*, vol. 58, no. 10, pp. 2032–2035, Oct. 2011.
[53] D. J. Sheskin, *Handbook of Parametric and Nonparametric Statistical Procedures*, 5th ed. Boca Raton, FL, USA: CRC Press, 2011, pp. 1280–1290.
[54] C. M. Bishop, *Neural Networks for Pattern Recognition*. London, U.K.: Oxford Univ. Press, 1995, pp. 106–109.
[55] G. Millonig *et al.*, "Liver stiffness is directly influenced by central venous pressure," *J. Hepatol*, vol. 52, no. 2, pp. 206–210, 2010.
[56] K. J. Parker, J. Ormachea, and Z. Hah, "Group versus phase velocity of shear waves in soft tissues," *Ultrason. Imag.*, vol. 40, no. 6, pp. 343–356, 2018.
[57] M. L. Palmeri, M. H. Wang, J. J. Dahl, K. D. Frinkley, and K. R. Nightingale, "Quantifying hepatic shear modulus *in vivo* using acoustic radiation force," *Ultrasound Med. Biol.*, vol. 34, no. 6, pp. 546–558, 2008.
[58] M. Tabaru, T. Azuma, and K. Hashiba, "Measurement of elastic properties of tissue by shear wave propagation generated by acoustic radiation force," *Jpn. J. Appl. Phys.*, vol. 49, no. 7S, 2010, Art. no. 07HF09.
[59] E. Bogin, Y. Avidar, M. Merom, S. Soback, and G. Brenner, "Biochemical changes associated with the fatty liver syndrome in cows," *J. Comparative Pathol.*, vol. 98, no. 3, pp. 337–347, 1988.
[60] W. Molee, M. Bouillier-Oudot, A. Auvergne, and R. Babilé, "Changes in lipid composition of hepatocyte plasma membrane induced by overfeeding in duck," *Comparative Biochem. Physiol. B, Biochem. Mol. Biol.*, vol. 141, no. 4, pp. 437–444, 2005.
[61] L. Théron *et al.*, "Modeling the relationships between quality and biochemical composition of fatty liver in mule ducks," *J. Animal Sci.*, vol. 90, no. 9, pp. 3312–3317, 2012.
[62] G. Millonig *et al.*, "Extrahepatic cholestasis increases liver stiffness (FibroScan) irrespective of fibrosis," *Hepatology*, vol. 48, no. 5, pp. 1718–1723, 2008.
[63] G. Montaldo, M. Tanter, J. Bercoff, N. Benech, and M. Fink, "Coherent plane-wave compounding for very high frame rate ultrasonography and transient elastography," *IEEE Trans. Ultrason., Ferroelectr., Freq. Control*, vol. 56, no. 3, pp. 489–506, Mar. 2009.

Manish Bhatt received the bachelor's degree in technology from the National Institute of Technology, Hamirpur, India, in 2011, and the Ph.D. degree in biomedical imaging from the Indian Institute of Science, Bengaluru, India, in 2016.

He is currently a Post-Doctoral Fellow with the University of Montreal Hospital Research Centre, Montreal, QC, Canada. His research interests are in ultrasound imaging, photoacoustics, inverse problems, and biomedical optics.

Marine A. C. Moussu is currently pursuing the Ph.D. degree with the Institut Fresnel, Marseille, France.

She was an Intern with the Laboratory of Biorheology and Medical Ultrasonics, University of Montreal Hospital Research Centre, during the course of this work. Her research interests are in wave physics applied to biomedical topics.

Boris Chayer received the bachelor's degree in electrical engineering and the master's degree in biomedical engineering from the École de Technologie Supérieure, Montreal, QC, Canada, in 2001 and 2007, respectively.

He was a Research Engineer with the Institut de Recherches Cliniques de Montreal, Montreal, for four years. In 2004, he joined the Laboratory of Biorheology and Medical Ultrasonics, University of Montreal Hospital Research Centre, Montreal. His current research interests are on quantitative ultrasound imaging, elastography, and biomedical phantom designs.

François Destrempes received the B.Sc. degree in mathematics from the University of Montreal, Montreal, QC, Canada, in 1985, the Ph.D. degree in mathematics from Cornell University, Ithaca, NY, USA, in 1990, and the Ph.D. degree in computer science from the University of Montreal, in 2006.

He was a Post-Doctoral Fellow with the Center de Recherches Mathématiques, University of Montreal, from 1990 to 1992. He was a Lecturer with Concordia University, Montreal, and an Assistant Professor of mathematics with the University of Ottawa, Ottawa, ON, Canada, the University of Toronto, Toronto, ON, Canada, and the University of Alberta, Edmonton, AB, Canada. He was a Post-Doctoral Fellow with the Laboratory of Biorheology and Medical Ultrasonics, University of Montreal Hospital Research Centre, Montreal, where he has been a Research Associate since 2008. He has authored or coauthored 36 articles and two book chapters. His current research interests include ultrasound imaging, segmentation of ultrasound images, quantitative ultrasound, and machine learning.

Marc Gesnik received the Engineering degree from the École Supérieure de Physique et de Chimie Industrielles de la Ville de Paris (ESPCI Paris), Paris, France, in 2014, the M.Sc. degree in physical acoustics from Paris VII University, Paris, in 2014, and the Ph.D. degree from the Institut Langevin, CNRS–INSERM–ESPCI Paris, in 2017.

He is currently a Post-Doctoral Fellow with the University of Montreal Hospital Research Centre, Montreal, QC, Canada. His research interests include elastography, quantitative ultrasound imaging, functional ultrasound imaging, and photoacoustics.

Louise Allard received the Ph.D. degree in social sciences from the University of Montreal, Montreal, QC, Canada, in 1993.

After working as a scientist at a Quebec Government Health Agency, Laval and Trois-Rivières, QC, Canada, she joined the Laboratory of Biorheology and Medical Ultrasonics, University of Montreal Hospital Research Centre, Montreal, to become a Research Coordinator in 2002. In 2018, she became a Research Associate in the same laboratory. She has also been acting for five years as the Technical Manager of the Experimental Imaging Platform at the University of Montreal Hospital Research Center. Her research interests include quantitative ultrasound applied to red blood cell aggregation and liver steatosis imaging, the design of medical imaging vascular phantoms, and preclinical animal experiments.

An Tang received the M.D. degree from the University of Sherbrooke, Sherbrooke, QC, Canada, in 2000, and the M.Sc. degree in biomedical sciences from the University of Montreal, Montreal, QC, Canada, in 2012.

He completed the Radiology Residency Program with the University of Montreal in 2005. He pursued fellowship training in abdominal imaging with the University of Toronto, Toronto, ON, Canada, in 2006. From 2006 to 2011, he practiced as an Abdominal Radiologist with the University of Montreal Hospital, Montreal. He pursued a research fellowship in liver elastography with the University of California at San Diego, La Jolla, CA, USA, from 2011 to 2012. He is currently a Clinical Researcher with the University of Montreal Hospital Research Centre, Montreal, and an Associate Professor of radiology with the University of Montreal. His current research interests include imaging-based techniques for diagnosis and monitoring of chronic liver disease, including biomarkers of liver fat, inflammation, and fibrosis.

Guy Cloutier (S'89–M'90–SM'07) received the B.Eng. degree in electrical engineering from the Université du Québec à Trois-Rivières, Trois-Rivières, QC, Canada, in 1984, and the M.Sc. and Ph.D. degrees in biomedical engineering from the École Polytechnique of Montreal, Montreal, QC, Canada, in 1986 and 1990, respectively.

From 1990 to 1992, he was a Post-Doctoral Fellow with the Pennsylvania State University, State College, PA, USA, with Prof. K. Kirk Shung. He is currently the Director of the Laboratory of Biorheology and Medical Ultrasonics, University of Montreal Hospital Research Centre, Montreal, a Professor with the Department of Radiology, Radio-Oncology, and Nuclear Medicine, University of Montreal, and a member of the Institute of Biomedical Engineering, University of Montreal. He has authored more than 200 peer-reviewed articles, holds several patents, and has licensed four technologies. His research interests are in quantitative ultrasound imaging, quasi-static and dynamic ultrasound elastography, development of multiphysics imaging methods, and biomechanical modeling.

Dr. Cloutier was a recipient of the National Scientist Award of the Fonds de la Recherche en Santé du Québec from 2004 to 2009. He is currently an Associate Editor-in-Chief of the IEEE TRANSACTIONS ON ULTRASONICS, FERROELECTRICS, AND FREQUENCY CONTROL, an Academic Editor of *PLOS One*, an Invited Associate Editor of *Medical Physics*, and an Editorial Board Member of *Current Medical Imaging Reviews*, and was a Member of the International Advisory Editorial Board of *Ultrasound in Medicine and Biology* for 15 years.